The Astrophysical Journal, 734:18 (9pp), 2011 June 10 doi:10.1088/0004-637X/734/1/18

RE-ACCELERATION OF NON-THERMAL PARTICLES AT WEAK COSMOLOGICAL SHOCK WAVES

Hyesung Kang[1] and Dongsu Ryu[2,3]
[1] Department of Earth Sciences, Pusan National University, Pusan 609-735, Republic of Korea; kang@uju.es.pusan.ac.kr
[2] Department of Astronomy and Space Science, Chungnam National University, Daejeon, Republic of Korea; ryu@canopus.cnu.ac.kr
Received 2011 February 13; accepted 2011 March 28; published 2011 May 20

ABSTRACT

We examine diffusive shock acceleration (DSA) of the pre-existing as well as freshly injected populations of non-thermal, cosmic-ray (CR) particles at weak cosmological shocks. Assuming simple models for thermal leakage injection and Alfvénic drift, we derive analytic, time-dependent solutions for the two populations of CRs accelerated in the test-particle regime. We then compare them with the results from kinetic DSA simulations for shock waves that are expected to form in intracluster media and cluster outskirts in the course of large-scale structure formation. We show that the test-particle solutions provide a good approximation for the pressure and spectrum of CRs accelerated at these weak shocks. Since the injection is extremely inefficient at weak shocks, the pre-existing CR population dominates over the injected population. If the pressure due to pre-existing CR protons is about 5% of the gas thermal pressure in the upstream flow, the downstream CR pressure can absorb typically a few to 10% of the shock ram pressure at shocks with a Mach number $M \lesssim 3$, yet the re-acceleration of CR electrons can result in a substantial synchrotron emission behind the shock. The enhancement in synchrotron radiation across the shock is estimated to be about a few to several for $M \sim 1.5$ and 10^2–10^3 for $M \sim 3$, depending on the detail model parameters. The implication of our findings for observed bright radio relics is discussed.

Key words: acceleration of particles – cosmic rays – galaxies: clusters: general – shock waves

Online-only material: color figures

1. INTRODUCTION

Cosmological shock waves result from supersonic flow motions induced by hierarchical clustering during the large-scale structure formation in the universe (Miniati et al. 2000; Ryu et al. 2003). According to studies based on cosmological hydrodynamic simulations, the shocks formed by the merger of subclumps, infall of matter, and internal flow motion in intracluster media (ICM) and cluster outskirts are relatively weak with a Mach number of $M \lesssim$ a few (Ryu et al. 2003; Pfrommer et al. 2006; Kang et al. 2007; Skillman et al. 2008; Hoeft et al. 2008; Vazza et al. 2009). Indeed, observations of X-ray shocks (e.g., Markevitch et al. 2002, 2005; Markevitch & Vikhlinin 2007) and radio relics (e.g., Bagchi et al. 2006; Finoguenov et al. 2010; van Weeren et al. 2010) indicate that the estimated Mach number of observed shocks in cluster environments is consistent with such theoretical predictions.

Suprathermal particles are known to be produced as an inevitable consequence of the formation of collisionless shocks in tenuous plasmas and they can be further accelerated to become cosmic rays (CRs) through interactions with resonantly scattering Alfvén waves in the converging flow across a shock (Bell 1978a; Drury 1983; Malkov & Drury 2001). Detailed nonlinear treatments of diffusive shock acceleration (DSA) have predicted that at strong shocks a significant fraction of the shock kinetic energy is transferred to CRs, inducing highly non-linear back-reactions from CRs to the underlying flow (e.g., Amato & Blasi 2006; Vladimirov et al. 2006; Kang & Jones 2007). Multiband observations of non-thermal radio to γ-ray emissions have confirmed the acceleration of CR electrons and protons up to 100 TeV at young supernova remnants (e.g., Parizot et al. 2006; Reynolds 2008; Abdo et al. 2010).

The presence of non-thermal particles, especially electrons, in clusters of galaxies, has been inferred from observations of synchrotron emission from radio halos and relics (see, e.g., Carilli & Taylor 2002; Govoni & Feretti 2004 for review). Since the matter in ICM and cluster outskirts first should have gone through accretion shocks of high Mach number around nonlinear structures and then through weaker shocks due to mergers and flow motion (Ryu et al. 2003; Kang et al. 2007), DSA should be responsible for at least a part of the CR production. Non-thermal particles can also be produced via turbulent acceleration (see, e.g., Cassano & Brunetti 2005; Brunetti & Lazarian 2007). According to recent *Fermi* observations of γ-ray emission from galaxy clusters, however, the pressure due to CR protons cannot exceed $\sim$10% of the gas thermal pressure (Abdo et al. 2010; Donnert et al. 2010).

At weak shocks with $M \lesssim$ a few, DSA is known to be rather inefficient and the CR pressure remains dynamically insignificant, partly because the injection from thermal to non-thermal particles is inefficient (e.g., Kang et al. 2002). In such a test-particle regime, the downstream CR spectrum takes the power-law form of $f_2(p) \propto p^{-q}$, where the spectral slope, q, depends on the velocity jump across the shock (Drury 1983). Recently, Kang & Ryu (2010) suggested analytic, time-dependent solutions for the test-particle CR spectrum, using results from DSA simulations in which particles are injected via a thermal leakage process at quasi-parallel shocks and accelerated to ever increasing maximum momentum, $p_{\rm max}(t)$. They found that at weak shocks expected to form in ICM and cluster outskirts, indeed, much less than $\sim 10^{-3}$ of particles are injected into CRs and much less than $\sim$1% of the shock ram pressure is converted into the downstream pressure of CR protons, so the particle acceleration is virtually negligible.

However, the recent discovery of very bright radio relics associated with weak shocks of $M \lesssim$ a few (e.g., Bagchi et al. 2006; Finoguenov et al. 2010; van Weeren et al. 2010) suggests

[3] Author to whom any correspondence should be addressed.

that, contrary to the expectation, DSA should operate at weak shocks in cluster environments. One way to explain this is to presume that the relics form in media with *pre-existing* CRs which were produced by DSA during previous shocks and/or by turbulent acceleration. The existence of pre-exiting CRs alleviates the problem of inefficient injection at weak shocks.

In this paper, we examine the DSA at weak cosmological shocks in the presence of pre-existing CRs. First, the properties of weak shocks in ICM and cluster outskirts are briefly reviewed in Section 2. Analytic, time-dependent solutions for the acceleration of the pre-existing and freshly injected populations of CRs in the test-particle regime are described in Section 3, while the numerical solutions from kinetic DSA simulations are presented in Section 4. The synchrotron radiation from CR electrons accelerated at these shocks is discussed in Section 5. Finally, a brief summary is given in Section 6.

2. SHOCK WAVES IN ICM AND CLUSTER OUTSKIRTS

Shock waves in the large-scale structure of the universe have been studied in detail using various hydrodynamic simulations for the cold dark matter cosmology with cosmological constant (ΛCDM; Ryu et al. 2003; Pfrommer et al. 2006; Kang et al. 2007; Skillman et al. 2008; Hoeft et al. 2008; Vazza et al. 2009). It was found that shocks with Mach numbers typically up to $M \sim 10^3$ and speed up to $u_s \sim$ a few $\times 1000$ km s^{-1} in the present universe ($z = 0$). In ICM and cluster outskirts, however, shocks are expected to have lower Mach numbers, because they form in the hot gas of $kT \gtrsim$ keV.

To examine the characteristics of shocks in ICM and cluster outskirts, we analyze the shocks with a pre-shock gas temperature of $T_1 > 10^7$ K. The cosmic web is filled with ionized plasma, the intergalactic medium (Cen & Ostriker 1999; Kang et al. 2005). Hot gas with $T > 10^7$ K is found mostly in ICM and cluster outskirts, and the warm hot intergalactic medium with 10^5 K $< T < 10^7$ K is distributed mostly in filaments. Diffuse gas with $T < 10^5$ K resides mainly in sheet-like structures and voids. Shocks were found in a simulation of the *WMAP*1-normalized ΛCDM cosmology that employed the following parameters: $\Omega_b = 0.048$, $\Omega_m = 0.31$, $\Omega_\Lambda = 0.69$, $h \equiv H_0/(100\,\mathrm{km\,s^{-1}\,Mpc^{-1}}) = 0.69$, $\sigma_8 = 0.89$, and $n = 0.97$. The simulation was performed using a particle-mesh/Eulerian hydrodynamic cosmology code (Ryu et al. 1993). Detailed descriptions for numerical setup and input physical ingredients can be found in Cen & Ostriker (2006). The procedure for identifying shocks was described in detail in Ryu et al. (2003).

Figure 1 shows the surface area of shocks with $T_1 > 10^7$ K per Mach number interval in the entire simulation volume, normalized by volume. Here, S is given in units of $(h^{-1}\,\mathrm{Mpc})^{-1}$. The quantity S provides a measure of shock frequency or the inverse of the mean comoving distance between shock surfaces. To avoid confusion from complex flow patterns and shock surface topologies associated with very weak shocks, only those portions of shock surfaces with $M \geqslant 1.5$ are shown. We also calculated the incident shock kinetic energy flux, $F_\phi = (1/2)\rho_1 u_s^3$, where ρ_1 is the pre-shock gas density, and then the kinetic energy flux through shock surfaces per Mach number interval, normalized by simulation volume, $dF_\phi(M)/dM$. Figure 1 shows $dF_\phi(M)/dM$. As expected, the Mach number of the shocks formed in ICM and cluster outskirts is small, typically $M \lesssim 3$. The frequency increases to the weakest possible shocks with $M \sim 1$. The kinetic energy flux through shock surfaces is larger for weaker shocks; that is, weaker shocks process more shock energy, confirming the energetic dominance of weak shocks in cluster environments.

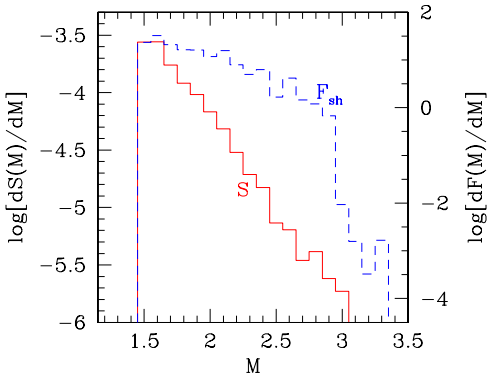

Figure 1. Surface area of shocks in ICM and cluster outskirts, S (red solid line), and kinetic energy flux passed through surfaces of the shocks, $F_{\rm sh}$ (blue dashed line), as a function of Mach number M at $z = 0$. Only shocks with a pre-shock gas temperature of $T_1 \geqslant 10^7$ K are considered.

(A color version of this figure is available in the online journal.)

3. ANALYTIC TEST-PARTICLE SPECTRUM

In the kinetic DSA approach for quasi-parallel shocks, the following diffusion–convection equation for the pitch-angle-averaged distribution function of CRs, $f(x, p, t)$, is solved along with suitably modified gasdynamic equations:

$$\frac{\partial f}{\partial t} + (u + u_w)\frac{\partial f}{\partial x} = \frac{p}{3}\frac{\partial (u + u_w)}{\partial x}\frac{\partial f}{\partial p} + \frac{\partial}{\partial x}\left[\kappa(x, p)\frac{\partial f}{\partial x}\right], \quad (1)$$

where $\kappa(x, p)$ is the spatial diffusion coefficient along the direction parallel to the mean magnetic field and u_w is the drift speed of the local Alfvénic wave turbulence with respect to the plasma (Skilling 1975). The scattering by Alfvén waves tends to isotropize the CR distribution in the wave frame, which may drift upstream at the Alfvén speed, v_A, with respect to the bulk plasma, so the wave speed is set as $u_w = -v_A$ upstream of shock and $u_w = 0$ downstream.

In the test-particle regime where the feedback due to CR pressure is negligible, the downstream CR distribution can be described with a power-law spectrum, $f_2(p) \propto p^{-q}$, and the slope is given by

$$q = \frac{3(u_1 - v_A)}{u_1 - v_A - u_2} = \frac{3\sigma\left(1 - M_A^{-1}\right)}{\left(\sigma - 1 - \sigma M_A^{-1}\right)}, \quad (2)$$

where u_1 and u_2 are the upstream and downstream flow speeds, respectively, in the shock rest frame, $\sigma = u_1/u_2 = \rho_2/\rho_1$ is the shock compression ratio, and $M_A = u_1/v_A$ is the upstream Alfvén Mach number with $v_A = B_1/\sqrt{4\pi\rho_1}$ (Drury 1983; Kang & Ryu 2010). The test-particle power-law slope q can be calculated as a function of shock Mach number M with $\sigma = [(\gamma_g + 1)M^2]/[(\gamma_g - 1)M^2 + 2]$, which becomes $4M^2/(M^2 + 3)$ for a gas adiabatic index $\gamma_g = 5/3$, and $M_A = M/\delta$. Here, $\delta \equiv v_A/c_s$ is the Alfvén speed parameter, where c_s is the upstream sound speed. The maximum momentum of CR protons achieved by the shock age of t can be estimated as

$$p_{\rm max}(t) \approx m_p c\left[\frac{\left(1 - M_A^{-1}\right)\left(\sigma - 1 - \sigma M_A^{-1}\right)}{3\sigma\left(2 - M_A^{-1}\right)}\right]\frac{u_s^2}{\kappa^*}t, \quad (3)$$

where $u_s = u_1$ is the shock speed (Drury 1983; Kang & Ryu 2010). Here, a Bohm-type diffusion coefficient,

$$\kappa(p) = \kappa^* \left(\frac{p}{m_p c}\right)\left(\frac{\rho_0}{\rho}\right), \quad (4)$$

is adopted, where $\kappa^* = m_p c^3/(3eB_0) = 3.13 \times 10^{22}(B_0/1\mu\mathrm{G})^{-1}\,\mathrm{cm^2\,s^{-1}}$ and B_0 and ρ_0 are the magnetic field strength and the gas density far upstream, respectively. In CR-modified shocks where CRs are dynamically non-negligible, in general, the upstream flow is decelerated in the precursor before it enters the gas subshock. We use the subscripts "0," "1," and "2" to denote the conditions far upstream, immediate upstream, and downstream of shock, respectively. Of course, in the test-particle limit, the distinction between far and immediate upstream quantities disappears, e.g., $\rho_0 = \rho_1$. In the limit of large M ($\sigma \approx 4$) and large M_A ($\delta \approx 0$), the maximum energy of CR protons can be approximated by

$$E_{\mathrm{max},p} \approx \frac{u_s^2 t}{8\kappa^*} m_p c^2 \approx 10^9\mathrm{GeV}\left(\frac{u_s}{10^3\ \mathrm{km\,s^{-1}}}\right)^2\left(\frac{t}{10^9\ \mathrm{yr}}\right)\left(\frac{B_0}{1\mu\ \mathrm{G}}\right). \quad (5)$$

The CR proton spectrum limited by the shock age is expected to have a cutoff at around $\sim p_{\max}(t)$ (see Section 3.3 for further discussion). We note that the diffusion length of these protons is $l_{\mathrm{max,p}} = \kappa(p_{\max})/u_s \approx (u_s t)/8 \approx 0.13\,\mathrm{Mpc}(u_s/1000\ \mathrm{km\,s^{-1}})(t/10^9\ \mathrm{yr})$, independent of B_0. If the linear size or the curvature of the shock is smaller than $l_{\mathrm{max,p}}$, the highest energy could be lower than $E_{\mathrm{max},p}$ limited by the shock age.

3.1. Pre-existing Population

As noted in the Introduction, it seems natural to assume that ICM and cluster outskirts contain pre-existing CRs. But their nature is not well constrained, except that $P_c \lesssim 0.1 P_g$, i.e., the pressure of CR protons is less than ~10% of the gas thermal pressure (e.g., Abdo et al. 2010; Donnert et al. 2010). With pre-existing CRs of spectrum $f_0(p)$ upstream of shock, the steady-state, test-particle solution of Equation (1) for the downstream CR distribution can be written as

$$f_2(p) = qp^{-q}\int_{p_{\mathrm{inj}}}^{p} p'^{q-1} f_0(p')dp' + f_{\mathrm{inj}}\left(\frac{p}{p_{\mathrm{inj}}}\right)^{-q}, \quad (6)$$

where q is the test-particle power-law slope given in Equation (2) (Bell 1978b; Drury 1983; Blasi 2004). Here, p_{inj} is the lowest momentum boundary above which particles can cross the shock, i.e., the injection momentum (see the next subsection). By this definition of p_{inj}, the CR distribution function, $f_0 = 0$ and $f_2 = 0$ for $p < p_{\mathrm{inj}}$. The first term on the right-hand side of Equation (6) represents the re-accelerated population of pre-existing CRs, while the second term represents the population of CRs freshly injected at the shock and will be discussed in the next subsection.

We adopt a power-law form, $f_0(p) = f_{\mathrm{pre}} \cdot (p/p_{\mathrm{inj}})^{-s}$, with a slope of $s = 4$–5, as the model spectrum for pre-existing CR protons. If pre-existing CRs were generated at previous shocks, a slope of $s = 4$–5 is achieved for $M \geqslant \sqrt{5}$ with $\delta = 0$ (see Equation (2)). On the other hand, if they are mainly the outcome of turbulent acceleration, the slope should be close to $s \sim 4$ (see, e.g., Chandran 2005). Then, the spectrum of re-accelerated CRs is obtained by direct integration:

$$f_2^{\mathrm{reac}}(p) = \begin{cases} [q/(q-s)][1-(p/p_{\mathrm{inj}})^{-q+s}]f_0(p), & \text{if } q \neq s \\ q\ln(p/p_{\mathrm{inj}})f_0(p), & \text{if } q = s. \end{cases} \quad (7)$$

If $q \neq s$, for $p \gg p_{\mathrm{inj}}$,

$$f_2^{\mathrm{reac}}(p) = \frac{q}{|q-s|} f_{\mathrm{pre}}\left(\frac{p}{p_{\mathrm{inj}}}\right)^{-r}, \quad (8)$$

where $r = \min(q, s)$. That is, if the spectral slope of pre-existing CRs is softer than the test-particle slope ($s > q$), the re-accelerated CR spectrum gets flattened to p^{-q} by DSA; in the opposite case ($s < q$), the re-accelerated CR spectrum is simply amplified by the factor of $q/(q-s)$ and retains the same slope as the slope of pre-existing CRs.

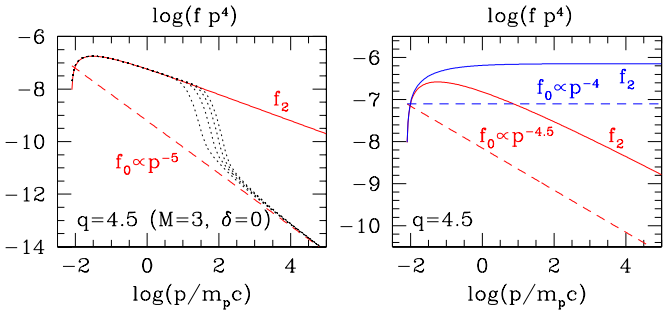

Figure 2. Steady-state solution for the downstream CR spectrum, $f_2^{\mathrm{reac}}(p)$, given in Equation (7) (sold lines), accelerated from an upstream CR spectrum, $f_0(p) \propto p^{-s}$ (dashed lines). A shock with Mach number $M = 3$ is considered, so the test-particle slope is $q = 4.5$ (with $\delta \equiv v_A/c_s = 0$). The CR injection is ignored and the distribution function $f(p)p^4$ is plotted. Left: the case with a slope of $s = 5$. The dotted lines show the time-dependent solution at the shock location, $f_s(p)$, from the corresponding DSA simulation. Right: the case with a slope of $s = 4$ and 4.5.

(A color version of this figure is available in the online journal.)

Figure 2 shows the re-accelerated CR distribution given in Equation (7) for an $M = 3$ shock in the presence of the pre-existing power-law CR spectrum with the slope $s = 4$ and 4.5 (right panel) and $s = 5$ (left panel). The Alfvénic drift is ignored ($\delta = 0$), so the test-particle slope is $q = 4.5$. Here, we adopted the following parameters: the upstream gas temperature $T_0 = 10^7$ K and the injection parameter $\epsilon_B = 0.25$, resulting in $p_{\mathrm{inj}} = 8.0 \times 10^{-3} m_p c$ (see the next subsection for details of our injection model).

The figure illustrates that for $p \gg p_{\mathrm{inj}}$, the CR amplification factor, $f_2(p)/f_0(p)$, approaches a constant, $q/(q-s) = 9$, in the case of $s = 4$, increases as $\ln(p/p_{\mathrm{inj}})$ in the case of $q = s = 4.5$, and scales as $(p/p_{\mathrm{inj}})^{s-q}$ in the case of $s = 5$. For instance, the factor becomes $f_2/f_0 = 32$ and 310 at $p/m_p c = 10$ for $s = 4.5$ and 5, respectively. We point out that these values of the CR amplification factor are substantially larger than those expected for the adiabatic compression across the shock. With pre-existing CRs of $f_0 \propto p^{-s}$, the amplification factor due to the adiabatic compression is given by

$$f_2^{\mathrm{adb}}/f_0 = \sigma^{s/3} \quad (9)$$

in the test-particle regime, so the adiabatic amplification factor is $f_2^{\mathrm{adb}}/f_0 = 4.3$, 5.2, and 6.2 for $s = 4$, 4.5, and 5, respectively, for a Mach 3 shock. Note that the adiabatic compression does not change the slope of the CR spectrum.

The left panel of Figure 2 also shows the time evolution of the CR distribution at the shock location, $f_s(p,t)$, from a DSA simulation for the same set of parameters (see Section 4 for details of DSA simulations). The CR injection was turned off for this particular simulation in order to compare the analytic and numerical solutions only for pre-existing CRs. This demonstrates that the time-dependent solution asymptotes to the steady-state solution in Equation (7).

3.2. Injected Population

Because complex plasma interactions among CRs, waves, and the underlying gas flow are not yet fully understood, it is not possible to make a precise quantitative prediction for the injection process from first principles (e.g., Malkov & Drury 2001). Here, we adopt a phenomenological injection model that can emulate the thermal leakage process through which particles above a certain injection momentum $p_{\rm inj}$ cross the shock and get injected to the CR population (Kang et al. 2002; Kang & Ryu 2010). Then, the CR distribution function at $p_{\rm inj}$ is anchored to the downstream Maxwellian distribution as

$$f_{\rm inj} = f(p_{\rm inj}) = \frac{n_2}{\pi^{1.5}} p_{\rm th}^{-3} \exp\left(-Q_{\rm inj}^2\right), \quad (10)$$

where n_2 is the downstream proton number density. Here, $p_{\rm inj}$ and $Q_{\rm inj}$ are defined as

$$Q_{\rm inj}(M) \equiv \frac{p_{\rm inj}}{p_{\rm th}} \approx 1.17 \frac{m_p u_2}{p_{\rm th}} \left(1 + \frac{1.07}{\epsilon_B}\right) \left(\frac{M}{3}\right)^{0.1}, \quad (11)$$

where $p_{\rm th} = \sqrt{2 m_p k_B T_2}$ is the thermal peak momentum of the downstream gas with a temperature of T_2 and k_B is the Boltzmann constant. We note that the functional form of $Q_{\rm inj}$ was adopted to represent an "effective" injection momentum, since particles in the suprathermal tail can cross the shock with a smoothly varying probability distribution (see Kang et al. 2002). One free parameter that controls the leakage process is the injection parameter, $\epsilon_B = B_0/B_\perp$, which is the ratio of the general magnetic field along the shock normal, B_0, to the amplitude of the downstream, magnetohydrodynamic wave turbulence, $B_\perp$. Although both plasma hybrid simulations and theories suggested that $0.25 \lesssim \epsilon_B \lesssim 0.35$ (Malkov & Völk 1998), the physical range of this parameter remains rather uncertain due to a lack of full understanding of relevant plasma interactions.

The second term in Equation (6) is fixed by q, $p_{\rm inj}$, and $f_{\rm inj}$. The fraction of particles injected into the CR population can be estimated analytically as well:

$$\xi \equiv \frac{n_{\rm CR}}{n_2} = \frac{4}{\sqrt{\pi}} Q_{\rm inj}^3 \exp\left(-Q_{\rm inj}^2\right) \frac{1}{q-3}, \quad (12)$$

which is fixed only by $Q_{\rm inj}$ and q. The injection fraction depends strongly on ϵ_B (through $Q_{\rm inj}$) for weak shocks with $M \lesssim 5$ (see also Kang & Ryu 2010). For example, it varies from 5×10^{-5} to 10^{-3} for $\epsilon_B = 0.25$–0.3 for shocks with $M = 3$.

3.3. Cosmic-ray Spectrum for Weak Shocks

Kang & Ryu (2010) demonstrated that the *time-dependent*, test-particle solutions of the downstream CR distribution can be represented by the steady-state, test-particle solutions with an exponential cutoff (Caprioli et al. 2009) if the cutoff momentum is set as $p^* \approx 1.2\, p_{\rm max}(t)$ with $p_{\rm max}(t)$ in Equation (3). Here, we suggest that the same cutoff would be applied to the spectrum of re-accelerated CRs. Then, the CR distribution at the shock location, x_s, originating from both the pre-existing and freshly injected populations can be approximated by

$$f_s(p,t) \equiv f_2(x_s, p, t) \approx \left[f_2^{\rm reac}(p) + f_{\rm inj} \cdot \left(\frac{p}{p_{\rm inj}}\right)^{-q} \right] \cdot \exp\left[-qC(z)\right], \quad (13)$$

where $f_2^{\rm reac}(p)$ is given in Equation (7) and $z = p/p^*$. The function $C(z)$ is defined as

$$C(z) = \int_{z_{\rm inj}}^{z} \frac{dz'}{z'} \frac{1}{\exp(1/z') - 1}, \quad (14)$$

where $z_{\rm inj} = p_{\rm inj}/p^*$ (Kang & Ryu 2010). Of course, for $p > p^*$, the acceleration is limited by the shock age and so pre-existing CRs will be simply advected downstream, resulting in $f_s(p) \approx f_0(p)$. These particles, however, do not make any significant contribution to the downstream CR pressure if the pre-existing power-law spectrum has a slope of $s > 4$ (see below).

4. COMPARISON WITH NUMERICAL SOLUTIONS

4.1. Setup for DSA Simulations

We carried out kinetic DSA simulations in order to test the time-dependent features of the test-particle solution in Equation (13). Also for shocks with typically $M \gtrsim$ a few, the evolution of CR-modified shocks should be followed by DSA simulations because the non-linear feedback of CRs becomes important (Kang & Ryu 2010). We used the Cosmic-Ray Acceleration SHock (CRASH) code for quasi-parallel shocks, in which the diffusion–convection equation (1) is solved along with the gasdynamic equation modified for the effects of the CR pressure (Kang et al. 2002).

We considered shocks with a wide range of Mach numbers, $M = 1.5$–5, propagating into typical ICM and cluster outskirts of $T_0 = 10^7$ K; the sound speed, $c_s = 474\ {\rm km\,s^{-1}}$, the Alfvén speed, $v_A = \delta \cdot 474\ {\rm km\,s^{-1}}$, and the shock speed, $u_s = M \cdot 474\ {\rm km\,s^{-1}}$. With such parameterization, the gas density and pressure become arbitrary and need not be specified in the simulations. The diffusion in Equation (4) was used. In the code units, the diffusion coefficient is normalized with $\kappa_o = 10^3 \kappa^*$ for numerical simulations. Then, the length and timescales are given as $l_o = \kappa_o/u_s$ and $t_o = \kappa_o/u_s^2$, respectively. Since the flow structure and P_c profile evolve self-similarly, a specific physical value of κ_o (or B_0) matters only in the determination of $p_{\rm max}$ at a given simulation time. For instance, $p_{\rm max}/m_p c \approx 10^3$ is achieved by the termination time of $t/t_o = 10$ in our simulations. Simulations start with purely gasdynamic shocks initially at rest at $x_s = 0$, and the gas adiabatic index is $\gamma_g = 5/3$.

As for the pre-existing CRs, we adopted $f_0(p) = f_{\rm pre}(p/p_{\rm inj})^{-s}$ for their spectrum. The amplitude, $f_{\rm pre}$, is set by the ratio of the upstream CR to gas pressure, $R \equiv P_{c,0}/P_{g,0}$, and we consider $R = 0.01$–0.1. We note that with the same value of R, the amplitude $f_{\rm pre}$ is larger for a softer pre-existing spectrum, i.e., larger s. To examine the effects of Alfvénic drift, in addition to the models with $\delta = 0$, we consider $\delta = 0.42$ to be a fiducial value, which corresponds to $E_B \sim 0.1 E_g$, i.e., the magnetic field energy density of ~10% of the gas thermal energy density. To be more specific, the assumed value

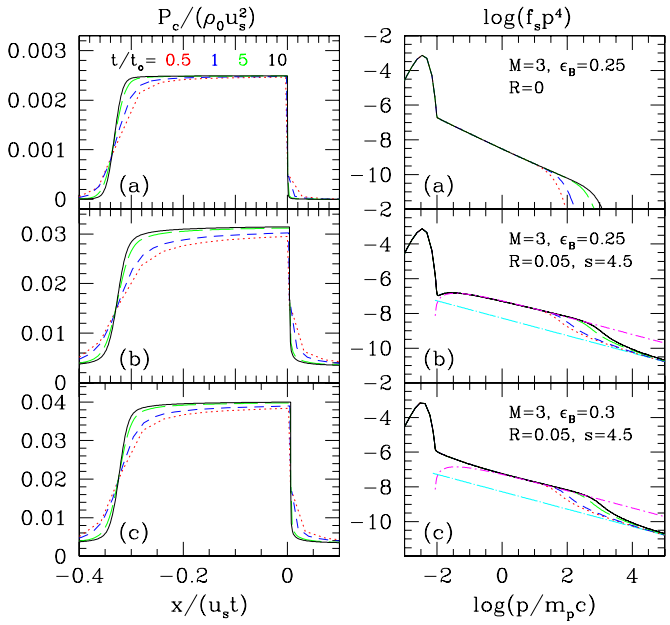

Figure 3. Time-dependent solution from DSA simulations of a Mach 3 shock. The CR pressure profile as a function of the similarity variable $x/(u_s t)$ (right panels) and the CR distribution at the shock location, $f_s(p)$, (left panels) at $t/t_o = 0.5$ (red dotted lines), 1 (blue dashed lines), 5 (green long-dashed line), and 10 (black solid lines) for three cases. The top panels show the case with the injection parameter $\epsilon_B = 0.25$ and without pre-existing CRs. The middle panels show the case with $\epsilon_B = 0.25$ and with pre-existing CRs: the ratio of the upstream, pre-existing CR to gas pressure is $R \equiv P_{c,0}/P_{g,0} = 0.05$ and the spectral slope of the pre-existing CRs is $s = 4.5$. The bottom panels show the case with the same pre-existing CRs, but with a higher injection rate, $\epsilon_B = 0.3$. All cases shown have $\delta \equiv v_A/c_s = 0.42$. In the left panels, the CR pressure is displayed in different vertical scales for clarity. In the right panels, for the cases (b) and (c), the (magenta) dot-dashed lines show the steady-state solution of the re-accelerated CRs, $f_2^{\rm reac}(p)$, in Equation (7), while the (cyan) dot-long-dashed lines show the pre-existing CR spectrum, $f_0(p)$, for comparison.

(A color version of this figure is available in the online journal.)

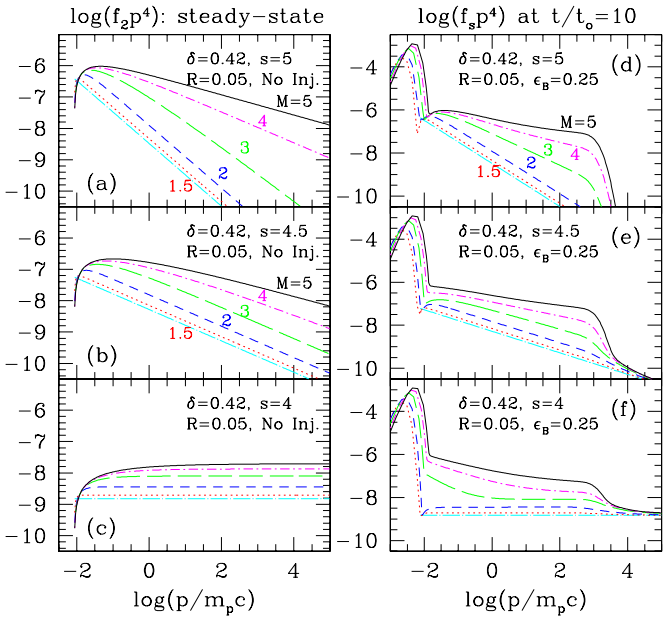

Figure 4. Left: steady-state solution of the re-accelerated CR spectrum (without injected population), $f_2^{\rm reac}(p)$, in Equation (7). Right: time-dependent solution of the CR distribution at the shock location, $f_s(p)$, at $t/t_o = 10$ from DSA simulations with the injection parameter $\epsilon_B = 0.25$. Three different spectral slopes of pre-existing CRs $s = 4$, 4.5, and 5 are considered. In all cases, $R = P_{c,0}/P_{g,0} = 0.05$ and $\delta = v_A/c_s = 0.42$. Results are shown for shocks with Mach number $M = 1.5$ (red dotted lines), 2 (blue dashed lines), 3 (green long-dashed lines), 4 (magenta dot-dashed line), 5 (black solid lines). The (cyan) dot-long-dashed lines plot the pre-existing CRs, $f_0(p)$.

(A color version of this figure is available in the online journal.)

of $v_A = \delta \cdot 474\,{\rm km\,s^{-1}} \approx 200\,{\rm km\,s^{-1}}$ corresponds to the Alfvén speed of the ICM with $B_0 = 1\mu$G and $n_{\rm H} = 1.2 \times 10^{-4}{\rm cm^{-3}}$. Finally, we consider $\epsilon_B = 0.25$–0.3 for the injection parameter.

4.2. CR Proton Spectrum and CR Pressure

Figure 3 shows the CR pressure profile and the CR distribution at the shock location, f_s, from DSA simulations for a Mach 3 shock. In the cases with pre-existing CRs in panels (b) and (c), the steady-state solution without injection given in Equation (7) (dot-dashed line) is also shown for comparison. As CRs are accelerated to ever higher energies ($p_{\rm max} \propto t$), the scale length of the CR pressure increases linearly with time, $l_d(p_{\rm max}) \propto u_s t$ (Kang et al. 2009). The left panels demonstrate that the CR pressure profile evolves in a self-similar fashion, depending approximately only on the similarity variable, $x/(u_s t)$. The right panels indicate that f_s can be well approximated with the form in Equation (13), i.e., the acceleration of pre-existing and injected CRs along with an exponential cutoff at $p_{\rm max}(t)$.

Comparing the cases in panels (a) and (b), we see that with the same injection parameter, the presence of pre-existing CRs results in higher downstream CR pressure, and that the re-accelerated pre-existing population dominates over the injected population. The presence of pre-existing CRs acts effectively as a higher injection rate than the thermal leakage alone, leading to a greatly enhanced CR acceleration efficiency. For the case with $\epsilon_B = 0.3$ in the (c) panels, the injection rate is much higher than that of the case with $\epsilon_B = 0.25$, yet the injected population makes a non-negligible contribution only near $p_{\rm inj}$.

In Figure 4, we compare the spectrum of re-accelerated CRs from the steady-state solutions without injection (left panels) and the CR spectrum at the shock location from the time-dependent solutions of DSA simulations at $t/t_o = 10$ (right panels), in order to demonstrate the relative importance of the acceleration of the pre-existing and the injected populations. Different values of M and s are considered, but $R = 0.05$, $\delta = 0.42$, and $\epsilon_B = 0.25$ are fixed. As noted before, with the same R, the amplitude $f_{\rm pre}$ of the pre-existing CR spectrum is larger for larger s, so the re-acceleration of the pre-existing population is relatively more important. The figure indicates that for most cases considered, the re-accelerated pre-existing population dominates over the injected population for the considered range of Mach number. Only for the cases with $s = 4$ and $M \gtrsim 3$, the freshly injected population makes a noticeable contribution.

Figure 5 shows the downstream CR pressure, $P_{c,2}$, relative to the shock ram pressure, $\rho_0 u_s^2$, and to the downstream gas thermal pressure, $P_{g,2}$, as a function of shock Mach number M for different values of R, s, and δ. Again, $\epsilon_B = 0.25$ in all the cases. As shown in the top panels, without pre-existing CRs, both $P_{c,2}/\rho_0 u_s^2$ and $P_{c,2}/P_{g,2}$ steeply increase with M, because both the injection and acceleration efficiencies depend strongly on M. For shocks with $M \gtrsim 5$, $P_{c,2}/(\rho_0 u_s^2) \gtrsim 0.1$ and the non-linear feedback begins to be noticeable. The feedback reduces the CR injection and saturates the CR acceleration, so $P_{c,2}$ from DSA simulations becomes smaller than the analytic estimates in the test-particle limit (see also Kang & Ryu 2010). Also

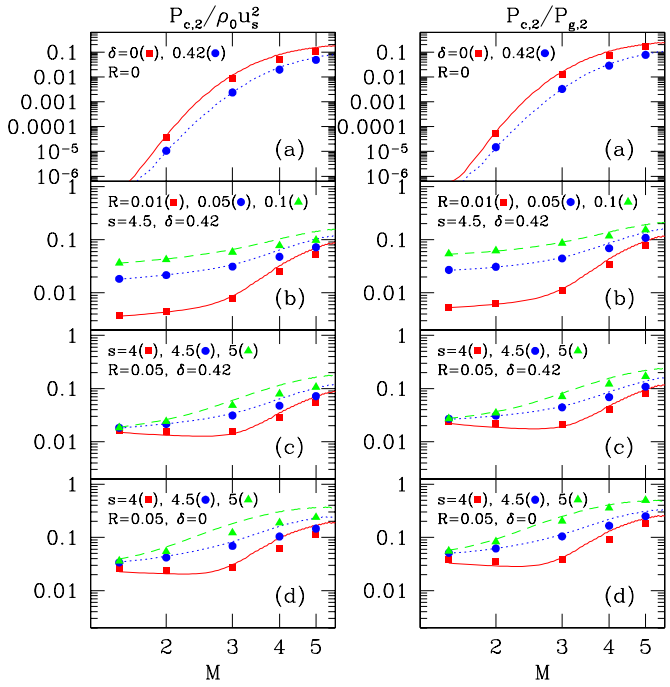

Figure 5. Ratios of the downstream CR pressure to the shock ram pressure (left panels) and to the downstream gas thermal pressure (right panels) for different model parameters. Lines show the ratios estimated from the analytic formula in Equation (13), while symbols show the time-asymptotic values from the corresponding DSA simulations at $t/t_o = 10$. The top panes show the cases without pre-existing CRs for two different $\delta \equiv v_A/c_s = 0$ and 0.42. The second panels from top show the cases with pre-existing CRs of different $R \equiv P_{c,0}/P_{g,0} = 0.01$, 0.05, and 0.1. The spectral slope of pre-existing CRs is $s = 4.5$, and $\delta = 0.42$ is adopted. The third panels from top show the cases with pre-existing CRs of different $s = 4$, 4.5 and $s = 5$. Other parameters are $R = 0.05$ and $\delta = 0.42$. The bottom panels show the same cases as the third panels except $\delta = 0$. In all cases, $\epsilon_B = 0.25$ is used.

(A color version of this figure is available in the online journal.)

the top panels compare the models with $\delta = 0$ and $\delta = 0.42$, demonstrating that the Alfvénic drift softens the accelerated spectrum and reduces the CR pressure.

In the (b) panels, the cases with different upstream CR pressure fractions are compared: $P_{c,2}$ increases almost linearly with R at shocks with $M \lesssim 3$ in the test-particle regime, while the CR acceleration begins to show a saturation effect for $M \gtrsim 4$. With pre-existing CRs, both $P_{c,2}/\rho_0 u_s^2$ and $P_{c,2}/P_{g,2}$ are substantially larger, compared to the case with $R = 0$, especially for $M \lesssim 3$, confirming the dominance of the re-accelerated pre-existing population over the injected population at weak shocks.

In the (c) panels, the cases with different pre-existing slopes are compared; with a softer spectrum (larger s), the amplitude $f_{\rm pre}$ is larger and the CR acceleration is more efficient, as described above with reference to Figure 4. In the (d) panels, we show the same cases as in the (c) panels except $\delta = 0$, again demonstrating the effects of Alfvénic drift.

These results indicate that at shocks with $M \lesssim 3$ in ICM and cluster outskirts, the downstream CR pressure is typically a few to 10% of either the shock ram pressure or the downstream gas thermal pressure. Even in the cases where the pre-existing CR population takes up to 10% of the gas thermal pressure in the upstream flow, $P_{c,2}/P_{g,2} \lesssim 0.1$ in the downstream flow. This is consistent with the *Fermi* upper limit (Abdo et al. 2010; Donnert et al. 2010).

5. CR ELECTRONS AND SYNCHROTRON RADIATION

Since DSA operates on relativistic particles of the same rigidity ($R = pc/Ze$) in the same way, both electrons and protons are expected to be accelerated at shocks. However, electrons lose energy, mainly by synchrotron emission and inverse Compton (IC) scattering, and the injection of postshock thermal electrons is believed to be much less efficient compared to protons.

The maximum energy of CR electrons accelerated at shocks can be estimated by the condition that the momentum gain per cycle by DSA is equal to the synchrotron/IC loss per cycle, i.e., $\langle \Delta p \rangle_{\rm DSA} + \langle \Delta p \rangle_{\rm rad} = 0$ (see Webb et al. 1984; Zirakashvili & Aharonian 2007). With an assumed Bohm-type diffusion coefficient, the electron spectrum has a cutoff at

$$p_{\rm cut} \approx \frac{m_e^2 c^2}{\sqrt{4e^3/27}} \frac{u_s}{\sqrt{q}} \sqrt{\frac{B_0}{B_{0,\rm eff}^2 + B_{2,\rm eff}^2}} \ \text{(in cgs units)}$$
$$\approx 340 \frac{\rm TeV}{c} \left(\frac{u_s}{10^3 \ {\rm km\,s^{-1}}^{-1}} \right) \times \sqrt{\frac{(B_0/1\,\mu{\rm G})}{q[(B_{0,\rm eff}/1\,\mu{\rm G})^2 + (B_{2,\rm eff}/1\,\mu{\rm G})^2]}}, \quad (15)$$

where $B_{\rm eff} = (B^2 + B_{\rm CMB}^2)^{1/2}$ with $B_{\rm CMB} = 3.24 \times 10^{-6}$ G is the effective magnetic field strength for synchrotron and IC coolings upstream and downstream of shock, and $\delta = 0$ is assumed. Note that the electron cutoff energy is a time-asymptotic quantity that depends only on the shock speed and the magnetic field strength, independent of the shock age. For a Mach 3 shock and $B_0 = 1\,\mu$G, for example, the shock jump condition gives $\sigma = 3$, $q = 4.5$ (with $\delta = 0$), and $B_2 = 3\,\mu$G (assuming $B \propto \rho$), resulting in a cutoff Lorentz factor of $\gamma_{\rm e,cut} = p_{\rm cut}/m_e c \approx 5.6 \times 10^7 \ (u_s/1000 \ {\rm km\,s^{-1}})$.

Thus, we may model the electron spectrum at the immediate downstream side of the shock as

$$f_{e,2}(p) \approx K_{e/p} \ f_{p,2}(p) \exp\left(-\frac{p^2}{p_{\rm cut}^2} \right), \quad (16)$$

where $f_{p,2}(p)$ is the downstream proton spectrum (Zirakashvili & Aharonian 2007). The electron-to-proton number ratio, $K_{e/p}$, is not yet constrained precisely by plasma physics (see, e.g., Reynolds 2008). Although $K_{e/p} \sim 10^{-2}$ is inferred for the Galactic CRs (Schlickeiser 2002), a much smaller value, $K_{e/p} \lesssim 10^{-4}$, is preferred for young supernova remnants (Morlino et al. 2009). However, $K_{e/p}$ for the pre-existing population in ICMs and cluster outskirts could be quite different from these estimates.

Next, from the electron spectrum in Equation (16), we consider the synchrotron emission. The averaged rate of synchrotron emission at photon frequency ν from a single relativistic electron with Lorentz factor γ_e can be written as

$$\langle P_\nu(\gamma_e) \rangle = \frac{4}{3} c \sigma_T \beta^2 U_B \gamma_e^2 \phi_\nu(\gamma_e), \quad (17)$$

where β is the particle speed in units of c, σ_T is the Thomson cross section, and U_B is the magnetic energy density (see, e.g., Shu 1991). The frequency distribution function, $\phi_\nu(\gamma_e)$, which satisfies the normalization $\int \phi_\nu(\gamma) d\nu = 1$, peaks at

$$\nu_{\rm peak} \approx \gamma_e^2 \nu_L = 280 \left(\frac{B}{1\,\mu{\rm G}} \right) \left(\frac{\gamma_e}{10^4} \right)^2 \ {\rm MHz}, \quad (18)$$

where $\nu_L = eB/(2\pi m_e c)$ is the Larmor frequency. If we approximate that the synchrotron radiation is emitted mostly at $\nu = \nu_{\rm peak}$ (i.e., $\phi_\nu(\gamma)$ is replaced by a delta function centered at $\nu = \nu_{\rm peak}$), the synchrotron volume emissivity from the CR electron number density, $n_e(\gamma_e)d\gamma_e = f_e(p)p^2dp$, becomes

$$J(\nu) \approx \frac{2}{3} c\sigma_T \beta^2 U_B \frac{\gamma_e}{\nu_L} n_e(\gamma_e), \tag{19}$$

with γ_e corresponding to the given $\nu_{\rm peak} = \nu$ in Equation (18). The ratio of the immediate downstream to upstream synchrotron emissivity at a given frequency ν can be written as

$$\frac{J_2(\nu)}{J_0(\nu)} \approx \frac{B_2}{B_0} \frac{\gamma_{e,2}^3 f_{e,2}(\gamma_{e,2})}{\gamma_{e,0}^3 f_{e,0}(\gamma_{e,0})}, \tag{20}$$

where $\gamma_{e,0}$ and $\gamma_{e,2}$ are the Lorenz factor that corresponds to the given $\nu_{\rm peak} = \nu$ in Equation (18) for upstream field B_0 and downstream field B_2, respectively.

For power-law spectra, the ratio $J_2(\nu)/J_0(\nu)$ can be written in a more intuitive form. If the ratio $K_{e/p}$ of the pre-existing population is comparable to or greater than that of the injected population, pre-existing electrons are more important than injected electrons at weak shocks of $M \lesssim 3$, as pointed out in the previous section. Then, the immediate downstream electron spectrum $f_{e,2}$ can be approximated by the distribution function in Equation (7) with a Gaussian cutoff, $\exp(-p^2/p_{\rm cut}^2)$. Again adopting $f_{e,0}(\gamma_e) \propto \gamma_e^{-s}$ for pre-existing CR electrons, the immediate downstream spectrum is $f_{e,2}(\gamma_e) \propto \gamma_e^{-r}$ (unless $q = s$) for $\gamma_e < \gamma_{\rm e,cut} \equiv p_{\rm cut}/m_e c$. Then, the ratio of the immediate downstream to upstream synchrotron emissivity at ν becomes

$$\begin{aligned}\frac{J_2(\nu)}{J_0(\nu)} &\approx \left(\frac{B_{2,\mu\rm G}^{(r-1)/2}}{B_{0,\mu\rm G}^{(s-1)/2}}\right) \left[\frac{f_{e,2}(\gamma_e)}{f_{e,0}(\gamma_e)}\right]_{\gamma_e=10^4} \left(\frac{\nu}{280\ \rm MHz}\right)^{(s-r)/2} \\ &\approx \sigma^{w(r-1)/2} B_{0,\mu\rm G}^{-(s-r)/2} \left[\frac{f_{e,2}(\gamma_e)}{f_{e,0}(\gamma_e)}\right]_{\gamma_e=10^4} \left(\frac{\nu}{280\ \rm MHz}\right)^{(s-r)/2},\end{aligned} \tag{21}$$

where $B_{0,\mu\rm G}$ and $B_{2,\mu\rm G}$ are the upstream and downstream magnetic field strengths, respectively, in units of μG. In the second step, we assumed that $B_2/B_0 = (\rho_2/\rho_0)^w = \sigma^w$, where $w = 1$ corresponds to $B \propto \rho$ implied by the diffusion model in Equation (4).

Figure 6 shows $f_{e,0}(\gamma_e)/f_{e,2}(\gamma_e)$ at $\gamma_e = 10^4$, and $(J_2/J_1)_{280} \equiv J_2(\nu)/J_0(\nu)$ at $\nu = 280$ MHz for $B_0 = 1\ \mu$G and $w = 1$ for the cases considered in Figure 5. Here, we assume that $K_{e/p}$ is the same for both the pre-existing and injected populations. Since the electron cutoff momentum is $\gamma_{\rm cut} \sim 10^8$ for the shock parameters considered here, the choice of $\gamma_e = 10^4$ and $\nu = 280$ MHz (see Equation (18)) as the representative values should be safe. As shown in Figure 5, for $M \lesssim 3$, the downstream CR proton pressure can absorb typically only a few to 10% of the shock ram pressure even for $R = 0.05$, yet the acceleration of CR electrons can result in a substantial enhancement in synchrotron radiation across the shock. Our estimation indicates that the enhancement factor, $(J_2/J_1)_{280}$, can be as large as several at shocks for $M \sim 1.5$, several 10 s for $M \sim 2$, and several 100 s for $M \sim 3$, depending on model parameters. This is partly due to the large enhancement of the electron population across the shock, $f_{e,2}/f_{e,0}$, which is typically an order of magnitude smaller than the ratio $(J_2/J_0)_{280}$. Additional

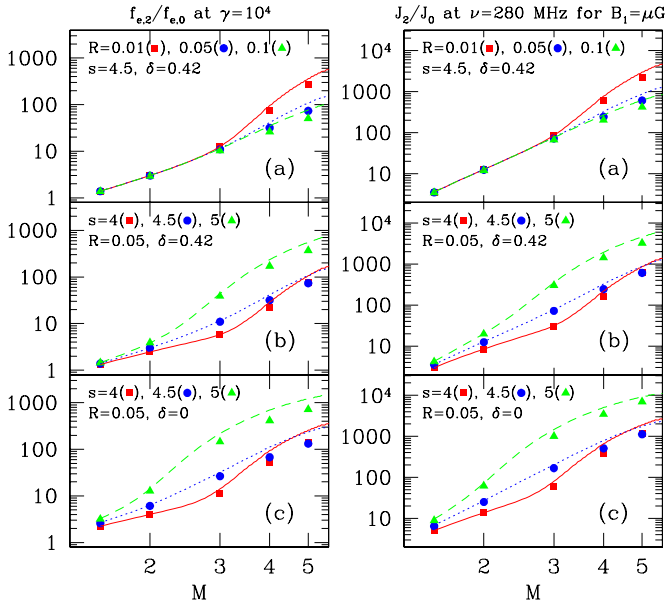

Figure 6. Ratios of the downstream to upstream CR electrons, $f_{e,2}(p)/f_{e,0}(p)$ at $p = 10^4\ m_e c$ (left panels) and the downstream to upstream synchrotron emissivity, $J_2(\nu)/J_0(\nu)$ at $\nu = 280$ MHz (right panels). The synchrotron emissivity was calculated by Equation (20) for the upstream and downstream magnetic field, $B_0 = 1\ \mu$G, and $B_2 = (\rho_2/\rho_0)B_0$, respectively. The cases are the same as in Figure 5 except without pre-existing CRs. See the caption of Figure 5 for different line and symbol types.

(A color version of this figure is available in the online journal.)

enhancement comes from the amplification of magnetic fields across the shock, B_2/B_0.

We note that for the compression of a uniform magnetic field, $B \propto \rho^{2/3}$, that is, $w = 2/3$. With this scaling, $(J_2/J_0)_{280}$ should be a bit smaller than that in Figure 6. However, it is also quite plausible that the downstream magnetic field is stronger than that expected for simple compression. It has been suggested that in shocks, especially strong ones, the downstream magnetic field is amplified by plasma instabilities (see, e.g., Lucek & Bell 2000; Bell 2004), although the existence of such instabilities has not been fully explored for weak shocks. Moreover, the magnetic field can be further amplified by the turbulence that is induced through a cascade of the vorticity generated behind shocks (Giacalone & Jokipii 2007; Ryu et al. 2008). In such cases, the ratio $(J_2/J_0)_{280}$ could be larger than that in Figure 6. In that sense, our estimate for the synchrotron enhancement factor may be considered to be a conservative one. We also note that with $s \geqslant r$ in Equation (21), $J_2(\nu)/J_0(\nu)$ is larger at higher frequencies, but smaller with larger B_0.

The above enhancement in synchrotron emission across the shock can be compared to the enhancement in a Bremsstrahlung X-ray. The Bremsstrahlung X-ray emissivity is given as $J_X \propto \rho^2\sqrt{T}$, so the ratio of the downstream to upstream emissivity can be written as

$$\frac{J_{X,2}}{J_{X,0}} = \sigma^2 \sqrt{\frac{T_2}{T_0}} = \left(\frac{4M^2}{M^2+3}\right)^{3/2} \left(\frac{5M^2-1}{4}\right)^{1/2}, \tag{22}$$

in the limit where the CR pressure does not modify the shock structure. The enhancement in Bremsstrahlung X-ray emission, $J_{X,2}/J_{X,0}$, is 3.6, 7.5, and 17 for $M = 1.5$, 2, and 3, respectively. These values are substantially smaller than $(J_2/J_0)_{280}$ shown in Figure 6. This implies that shocks in ICM and cluster outskirts may appear as radio relics, but not be detected in X-ray, for

instance, as in the case of CIZA J2242.8+5301 (van Weeren et al. 2010).

Since the synchrotron/IC cooling time scales as

$$t_{\rm rad} = \frac{2.45\times10^{13}\,{\rm yr}}{\gamma_e}\left(\frac{B_{\rm eff,2}}{1\,\mu{\rm G}}\right)^{-2} \quad (23)$$

(Webb et al. 1984), at the distance D behind the shock, the electron spectrum cuts off at $\gamma_{e,dn}$, which satisfies the condition, $t_{\rm rad}(\gamma_{e,dn}) \approx D/u_2$, and is smaller than $\gamma_{e,\rm cut}$ given in Equation (15). The ratio $J_2(\nu)/J_0(\nu)$ in Equation (21), for instance, is applicable to the downstream region where the electrons dominantly emitting synchrotron at ν have γ_e smaller than $\gamma_{e,\rm cut}$. The spatial width of the downstream region with electrons of γ_e becomes $d \approx u_2 t_{\rm rad}(\gamma_e) \propto \gamma_e^{-1}$. For instance, electrons radiating synchrotron at $\nu \sim 1$ GHz mostly have a Lorentz factor of $\gamma_e \approx 10^4$ in the magnetic field of $B_2 \sim$ a few μG, so the width of the synchrotron-emitting region behind the shock is $d \approx u_2 t_{\rm rad}(\gamma_e = 10^4) \sim 100$ kpc $(u_2/10^3\,{\rm km\,s^{-1}})$ as long as the shock age $t > t_{\rm rad}(\gamma_e = 10^4) \sim 10^8$ yr. This is indeed of order the width of bright radio relics such as CIZA J2242.8+5301 (van Weeren et al. 2010).

Moreover, from the fact that $d \propto \gamma_e^{-1}$, we can identify another feature in the integrated synchrotron spectrum. The volume-integrated electron spectrum, $F_{e,2}(\gamma_e) \propto f_{e,2}(\gamma_e)\cdot d \propto \gamma_e^{-(r+1)}$, steepens by one power of γ_e above the break Lorentz factor, $\gamma_{\rm e,br} \approx 2.45\times10^5\,(10^8\,{\rm yr}/t)\,(B_{\rm eff,2}/1\,\mu{\rm G})^{-2}$, where t is the shock age. Note that the break Lorentz factor is basically derived from the condition, $t = t_{\rm rad}$ in Equation (23) and so is independent of the shock speed. Hence, if $f_{e,2}(\gamma_e) \propto \gamma_e^{-r}$, in observations of unresolved sources, the integrated synchrotron emission, $S_\nu \propto \nu^{-\alpha}$, has a spectral slope of $\alpha = (r-3)/2$ for $\nu < \nu_{\rm br}$ and $\alpha = (r-2)/2$ for $\nu_{\rm br} \lesssim \nu \lesssim \nu_{\rm cut}$. Here, the two characteristic frequencies, $\nu_{\rm br}$ and $\nu_{\rm cut}$, correspond to the peak frequency in Equation (18) for $\gamma_{\rm e,br}$ and $\gamma_{\rm e,cut}$, respectively. Thus the spectral slope of the integrated spectrum just below the cutoff frequency is steeper than that of the resolved spectrum by 0.5.

6. SUMMARY

Cosmological shocks are expected to be present in the large-scale structure of the universe. They typically form with Mach numbers up to 10^3 and speeds up to a few 1000 km s^{-1} in the present universe. Shocks in ICM and cluster outskirts with relatively high X-ray luminosity, in particular, have the best chance to be detected, so they have started to be observed as X-ray shocks and radio relics (see the Introduction for references). Those shocks are mostly weak with small Mach numbers of $M \lesssim 3$, because they form in hot gas with $kT \gtrsim$ keV.

In this paper, we have studied DSA in weak cosmological shocks. Since the test-particle solutions could provide a simple yet reasonable description for weak shocks, we first suggested analytic solutions that describe the *time-dependent* DSA in the test-particle regime, including both the *pre-existing* and injected CR populations. We adopted a thermal leakage injection model to emulate the acceleration of suprathermal particles into the CR population, along with a simple transport model in which Alfvén waves drift relative to the bulk plasma upstream of the gas subshock. However, we did not follow the amplification of the magnetic field strength through CR streaming instabilities, which we expect would not be significant in weak shocks in the test-particle limit.

We then performed kinetic DSA simulations and compared the analytic and numerical solutions for wide ranges of model parameters relevant for shocks in ICM and cluster outskirts: the shock Mach number $M = 1.5$–5, the slope of the pre-existing CR spectrum $s = 4$–5, the ratio of the upstream CR to gas pressure $R = 0.01$–0.1, the injection parameter $\epsilon_B = 0.25$–0.3, and the Alfvénic speed parameter $\delta = 0$–0.42. The upstream gas was assumed to be fully ionized with $T_0 = 10^7$ K.

The main results can be summarized as follows.

1. For weak shocks with $M \lesssim 3$, the test-particle solutions given in Equation (13) should provide a good approximation for the time-dependent CR spectrum at the shock location. We note that the test-particle slope, q, in Equation (2) and the maximum momentum, $p_{\rm max}(t)$, in Equation (3) may include the Alfvénic drift effect.
2. For the injection parameter considered here, $\epsilon_B = 0.25$–0.3, the injection fraction is rather low, typically $\xi \sim 5\times10^{-5}$ to 10^{-3} for $M \lesssim 3$. The pre-existing CR population provides more particles for DSA than the freshly injected population. Hence, the pre-existing population dominates over the injected population. If there exist no CRs upstream ($R = 0$), the downstream CR pressure absorbs typically much less than ~1% of the shock ram pressure for $M \lesssim 3$. With pre-existing CRs that accounts for 5% of the gas thermal pressure in the upstream flow, the CR acceleration efficiency increases to a few to 10% for those weak shocks.
3. For the pre-existing population, the enhancement of the distribution function across the shock, $f_2(p)/f_1(p)$, at a given momentum is substantially larger than that expected from the simple adiabatic compression. Hence, with amplified magnetic fields downstream, the re-acceleration of pre-existing CR electrons can result in a substantial synchrotron radiation behind the shock. We estimated that the enhancement in synchrotron radiation across the shock, $J_2(\nu)/J_0(\nu)$, is about a few to several for $M \sim 1.5$, while it could reach up to 10^2–10^3 for $M \sim 3$, depending on the detail model parameters. This is substantially larger than the enhancement in X-ray emission.
4. Unlike protons, relativistic electrons lose energy by synchrotron emission and IC scattering behind the shock, resulting in a finite width of the synchrotron-emitting region. In ICM and cluster outskirts with μG fields, the radio synchrotron emission at $\nu \sim 1$ GHz originates mostly from the relativistic electrons with $\gamma_e \sim 10^4$, which cool in a timescale of $t_{\rm rad} \sim 10^8$ yr, so the width of the ~1 GHz synchrotron-emitting region is $d \approx u_2 t_{\rm rad} \sim 100\,{\rm kpc}\,(u_s/1000\ {\rm km\,s^{-1}})$ for a shock of age $t > t_{\rm rad}$.

We note, however, that our estimation of synchrotron enhancement was based on the DSA simulations which do not include cooling for electrons. A detailed comparison of observed radio relics and the synchrotron emission from the DSA simulations including energy losses via synchrotron emission and (IC) scattering (e.g., Kang 2011) will be presented elsewhere.

Finally, although the CRASH numerical code and our thermal leakage model were developed for quasi-parallel shocks, the main conclusions in this paper should be valid for quasi-perpendicular shocks as well. It is recognized that the injection may be less efficient and the self-excited waves are absent at perpendicular shocks. However, both of these problems are alleviated in the presence of pre-existing CRs and turbulence (Giacalone 2005; Zank et al. 2006). Thus, the diffusion approximation should be valid and the re-acceleration of pre-existing

CRs is similar in both kinds of shocks. We expect our results can be applied to, for instance, CIZA J2242.8+5301, the radio relic whose magnetic field direction inferred from the polarization observation is perpendicular to the shock normal.

The authors thank T. W. Jones and J. Cho for discussions. H.K. was supported by the Basic Science Research Program through the National Research Foundation of Korea (NRF) funded by the Ministry of Education, Science, and Technology (2010-0016425). D.R. was supported by the National Research Foundation of Korea through grant 2007-0093860.

REFERENCES

Abdo, A. A., et al. 2010, Science, 327, 1103
Amato, E., & Blasi, P. 2006, MNRAS, 371, 1251
Bagchi, J., Durret, F., Neto, G. B. L., & Paul, S. 2006, Science, 314, 791
Bell, A. R. 1978a, MNRAS, 182, 147
Bell, A. R. 1978b, MNRAS, 182, 443
Bell, A. R. 2004, MNRAS, 353, 550
Blasi, P. 2004, Astropart. Phys., 21, 45
Brunetti, G., & Lazarian, A. 2007, MNRAS, 378, 245
Caprioli, D., Blasi, P., & Amato, E. 2009, MNRAS, 396, 2065
Carilli, C. L., & Taylor, G. B. 2002, ARA&A, 40, 319
Cassano, R., & Brunetti, G. 2005, MNRAS, 357, 1313
Cen, R., & Ostriker, J. P. 1999, ApJ, 514, 1
Cen, R., & Ostriker, J. P. 2006, ApJ, 650, 560
Chandran, B. D. G. 2005, Phys. Rev. Lett., 95, 265004
Donnert, J., Dolag, K., Cassano, R., & Brunetti, G. 2010, MNRAS, 407, 1565
Drury, L. O'C. 1983, Rep. Prog. Phys., 46, 973
Finoguenov, A., Sarazin, C. L., Nakazawa, K., Wik, D. R., & Clarke, T. E. 2010, ApJ, 715, 1143
Giacalone, J. 2005, ApJ, 628, L37
Giacalone, J., & Jokipii, J. R. 2007, ApJ, 663, L41
Govoni, F., & Feretti, L. 2004, Int. J. Mod. Phys. D, 13, 1549
Hoeft, M., Bruggen, M., Yepes, G., Gottlober, S., & Schwope, A. 2008, MNRAS, 391, 1511
Kang, H. 2011, J. Korean Astron. Soc., 44, 49
Kang, H., & Jones, T. W. 2007, Astropart. Phys., 28, 232
Kang, H., Jones, T. W., & Gieseler, U. D. J. 2002, ApJ, 579, 337
Kang, H., & Ryu, D. 2010, ApJ, 721, 886
Kang, H., Ryu, D., Cen, R., & Ostriker, J. P. 2007, ApJ, 669, 729
Kang, H., Ryu, D., Cen, R., & Song, D. 2005, ApJ, 620, 21
Kang, H., Ryu, D., & Jones, T. W. 2009, ApJ, 695, 1273
Lucek, S. G., & Bell, A. R. 2000, MNRAS, 314, 65
Malkov, M. A., & Drury, L. O'C. 2001, Rep. Prog. Phys., 64, 429
Malkov, M. A., & Völk, H. J. 1998, Adv. Space Res., 21, 551
Markevitch, M., Gonzalez, A. H., David, L., Vikhlinin, A., Murray, S., Forman, W., Jones, C., & Tucker, W. 2002, ApJ, 567, L27
Markevitch, M., Govoni, F., Brunetti, G., & Jerius, D. 2005, ApJ, 627, 733
Markevitch, M., & Vikhlinin, A. 2007, Phys. Rep., 443, 1
Miniati, F., Ryu, D., Kang, H., Jones, T. W., Cen, R., & Ostriker, J. P. 2000, ApJ, 542, 608
Morlino, G., Amato, E., & Blasi, P. 2009, MNRAS, 392, 240
Parizot, E., Marcowith, A., Ballet, J., & Gallant, Y. A. 2006, A&A, 453, 387
Pfrommer, C., Springel, V., Enßlin, T. A., & Jubelgas, M. 2006, MNRAS, 367, 113
Reynolds, S. P. 2008, ARA&A, 46, 89
Ryu, D., Kang, H., Cho, J., & Das, S. 2008, Science, 320, 909
Ryu, D., Kang, H., Hallman, E., & Jones, T. W. 2003, ApJ, 593, 599
Ryu, D., Ostriker, J. P., Kang, H., & Cen, R. 1993, ApJ, 414, 1
Schlickeiser, R. 2002, Cosmic Ray Astrophysics (Berlin: Springer)
Shu, F. H. 1991, The Physics of Astrophysics, Vol. 1: Radiation (Mill Valley, CA: Univ. Science Books)
Skilling, J. 1975, MNRAS, 172, 557
Skillman, S. W., O'Shea, B. W., Hallman, E. J., Burns, J. O., & Norman, M. L. 2008, ApJ, 689, 1063
van Weeren, R., Röttgering, H. J. A., Brüggen, M., & Hoeft, M. 2010, Science, 330, 347
Vazza, F., Brunetti, G., & Gheller, C. 2009, MNRAS, 395, 1333
Vladimirov, A., Ellison, D. C., & Bykov, A. 2006, ApJ, 652, 1246
Webb, G. M., Drury, L. O'C., & Biermann, P. 1984, A&A, 137, 185
Zank, G. P., Li, G., Florinski, V., Hu, Q., Lario, D., & Smith, C. W. 2006, J. Geophys. Res., 111, 06108
Zirakashvili, V. N., & Aharonian, F. A. 2007, A&A, 465, 695